Performance Enhancement of pMOSFETs Depending on Strain, Channel Direction, and Material

Masaya Uchida, Yoshinari Kamakura, and Kenji Taniguchi
Division of Electrical, Electronic and Information Engineering, Osaka University
2-1 Yamada-oka, Suita, Osaka 565-0871, Japan
E-mail: uchida@qd.eie.eng.osaka-u.ac.jp

***Abstract* - In the framework of k·p band calculation, we investigate the modulation of the low-field mobility and the injection velocity of holes in Si- and Ge-channel pMOSFETs under the uniaxial and the biaxial strain. The contribution of the relaxation time and the conductivity effective mass modulation on the mobility enhancement is separately analyzed. Both the mobility and the injection velocity are enhanced most effectively by the uniaxial compressive strain along the ⟨110⟩ channel.**

1. INTRODUCTION

Strained Si MOSFETs have recently attracted great interest because of their promising electronic properties [1]. Figure 1 shows the example of the strained-Si *p*MOSFET technologies; Fig. 1(a) shows the combination of compressive SiGe strain and embedded SiGe geometry inducing a uniaxial compressive strain in the channel region [2], while Fig. 1(b) illustrates the *p*MOSFET fabricated on the relaxed $Si_{1-x}Ge_x$ substrate that can realize a large biaxial tensile strain [3]. Moreover, the Ge-channels, whose carrier mobility is known to be larger than Si [4], are also intensively studied now [5]. In these "channel engineering" technologies, which are considered to be necessary for further enhancement of MOSFET performance, the numerical simulation is essential especially for *p*-type channel design due to the complicated valence band structure. Many theoretical calculations of 2D hole gas have been recently reported, in most of which the modulation of low field mobility μ was the main interest [6,7].

In this study, we investigate not only μ but also the injection carrier velocity $v_{\rm inj}$, which becomes important in ballistic transport regime [8,9], for the strained Si- and Ge-channel *p*MOSFETs in the framework of the $\mathbf{k \cdot p}$ band calculation.

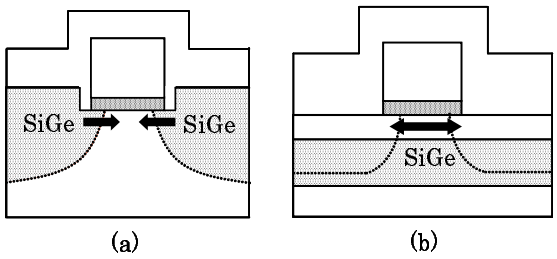

Fig. 1: Schematic view of the strained Si *p*MOSFET structures. (a) Uniaxial compressive strain [2] and (b) biaxial tensile strain [3].

2. CALCULATION METHOD

The subband structure for two dimensional hole states has been obtained by solving the wave equation based on the 6 × 6 Luttinger-Kohn Hamiltonian [10]. The effect of the strain was taken into account according to the theory of Bir-Pikus [11]. The values for the Luttinger parameters, Bir-Pikus deformation potentials, and the spin-orbit split-off energy were taken from [14,15]. The subband structure of *p*-type inversion layer was calculated by replacing $k_z \rightarrow -id/dz$ [12] in the Hamiltonian.

Figure 2 schematically illustrates the strain application methods considered in this study. Figure 2(a) shows the uniaxial compressive stress applied along the channel direction. We have assumed that the channel width is unchanged by the compressive strain, because the stress from the trench wall would prevent the lattice expansion in the direction of W. On the other hand, Fig. 2(b) shows the case of the biaxial tensile stress. It was assumed that the stress is applied uniformly over the channel layer. Then the strain is defined by the following equation:

$$e \equiv \frac{l - l_0}{l_0} , \qquad (1)$$

where l and l_0 are the crystal size after and before applying the stress, respectively.

This study focuses on the two quantities characterizing the carrier transport in two extreme cases as illustrated in Fig. 3. The low-field mobility μ has been a key parameter

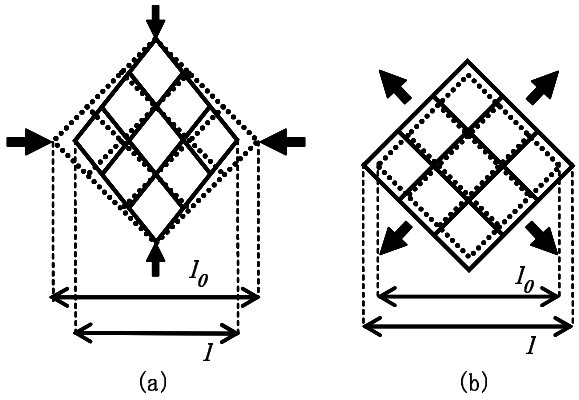

Fig. 2: Schematic view of the strain application methods. The dotted and the solid lines show the lattice before and after the stress application, respectively. The arrow is a direction vector of the stress. (a) Uniaxial compressive strain. (b) Biaxial tensile strain.

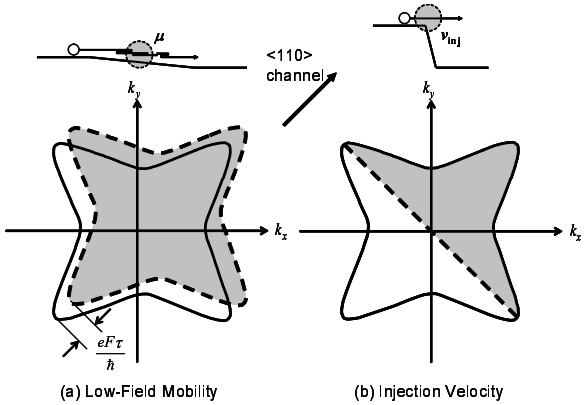

Fig. 3: Schematic view of the hole distribution in k-space assumed to evaluate low-field mobility μ (a) and injection velocity $v_{\rm inj}$ (b). The average group velocity of the holes distributed in the shaded area has been computed.

for determining the device performance, and is considered to have physical significance still in the nanoscale regime as a measure of the mean-free-path [13]. On the other hand, the injection carrier velocity at the source edge, $v_{\rm inj}$, is suggested to be important under full-ballistic transport condition [8,9]. In this study, these values have been numerically computed from the realistic subband structure using the following equations:

$$\mu_\theta \equiv \frac{\sum_{n\mathbf{k}} e\tau(n,\mathbf{k}) v_\theta^2(n,\mathbf{k}) \frac{\partial f_0}{\partial E}}{\sum_{n\mathbf{k}} f_0(E)} \ , \qquad (2)$$

$$v_{{\rm inj},\theta} \equiv \frac{1}{2} \frac{\sum_{n\mathbf{k}} |v_\theta(n,\mathbf{k})| f_0(E)}{\sum_{n\mathbf{k}} f_0(E)} \ , \qquad (3)$$

where e is the elementary charge, $\tau(n,\mathbf{k})$ is the momentum relaxation time for the hole with the in-plane wave vector $\mathbf{k}$ in the subband index n, $v_\theta(n,\mathbf{k})$ is the group velocity component along the θ-direction, and $f_0(E)$ is the equilibrium Fermi function for holes of energy $E(n,\mathbf{k})$. To perform the numerical integration in Eqs. (2) and (3), the 2D Brillouin zone was divided into 100×100 equally spaced mesh points, and the linear interpolation was adopted for the E-k relation. For $\tau(n,\mathbf{k})$, in this study, we have taken into account the acoustic phonon scattering only, for which the parameters given in [16] were used. In all the calculations presented later, the surface field $F_s = 1$ MV/cm, the hole sheet density $n_s = 1 \times 10^{13}$ cm^{-2}, and the temperature of 300 K were assumed.

3. RESULTS AND DISCUSSION

To examine the validity of the present model, the calculated mobilities were compared with experimental data [17] as shown in Fig. 4, where the good agreements are confirmed. Figures 5 and 6 show μ and $v_{\rm inj}$ as a function of uniaxial and biaxial strain for Si-pMOSFETs with the channel along $\langle 110 \rangle$ and $\langle 100 \rangle$ directions. The μ and $v_{\rm inj}$

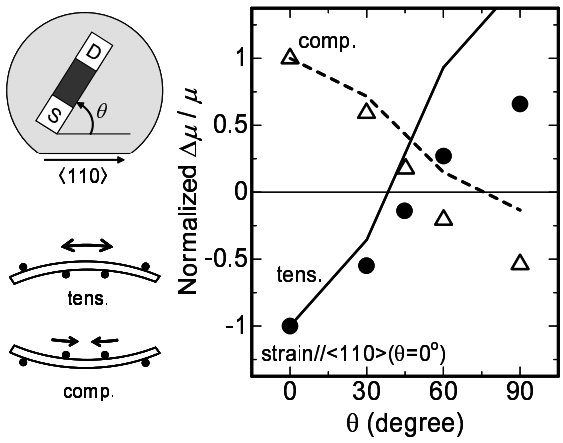

Fig. 4: Comparison of simulated (lines) and experimental [17] (symbols) hole mobilities under a uniaxial strain along $\langle 110 \rangle$ direction. The channel direction θ is varied from 0° to 90°.

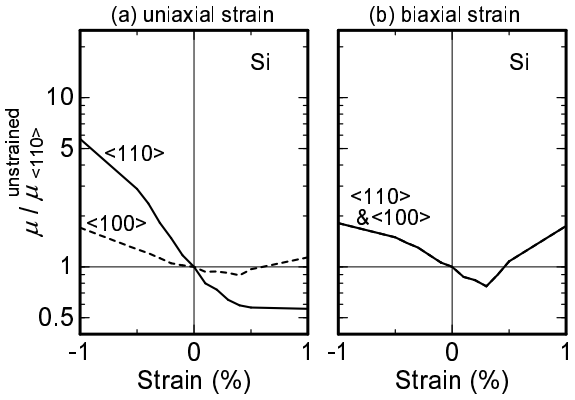

Fig. 5: Low field mobility of holes in Si-pMOSFETs with $\langle 110 \rangle$ (solid line) and $\langle 100 \rangle$ (dashed line) channel as a function of (a) uniaxial and (b) biaxial strain. The calculated results are normalized with respect to the values for the unstrained $\langle 110 \rangle$ channel.

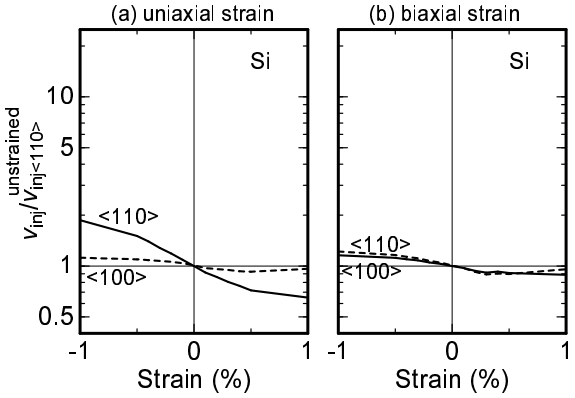

Fig. 6: Injection velocity of holes in Si-pMOSFETs with $\langle 110 \rangle$ (solid line) and $\langle 100 \rangle$ (dashed line) channel as a function of (a) uniaxial and (b) biaxial strain. The calculated results are normalized with respect to the values for the unstrained $\langle 110 \rangle$ channel.

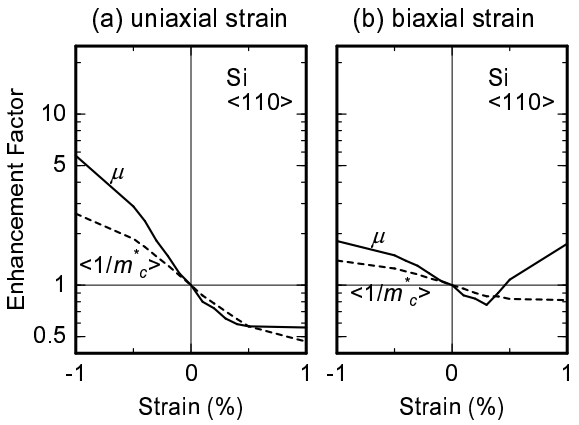

Fig. 7: μ (solid line) and the average effective conductivity mass $\langle 1/m_c^* \rangle$ (dashed line) of holes in $\langle 110 \rangle$ channel Si-pMOSFETs as a function of (a) uniaxial and (b) biaxial strain.

are significantly modulated by the uniaxial strain especially in the case of $\langle 110 \rangle$ channel, while the $\langle 100 \rangle$ channel is less sensitive to the strain.

The mobility modulation originates from the change of both the conductivity mass m_c^* and τ (remind that $\mu = e\tau/m_c^*$) [12,16]. In Fig. 7, we have evaluated the effective conductivity mass by substituting $e\tau = 1$ into Eq. (2) as

$$\left\langle \frac{1}{m_c^*} \right\rangle_\theta \equiv \frac{\sum_{n\mathbf{k}} v_\theta^2(n,\mathbf{k}) \frac{\partial f_0}{\partial E}}{\sum_{n\mathbf{k}} f_0(E)} \ . \qquad (4)$$

The modulation of $v_{\rm inj}$ shows a strong correlation with m_c^*. In addition, μ is also affected by τ, which increases significantly under the uniaxial compressive strain through the subband splitting (see Fig. 8 (a)) and the consequent suppression of the intersubband scattering. On the other hand, as shown in Fig. 7 (b), μ decreases under the small biaxial tensile strain. This is because the energy splitting between the ground and first exited subbands once decreases and then increases with the biaxial tensile strain as confirmed in Fig. 8 (b).

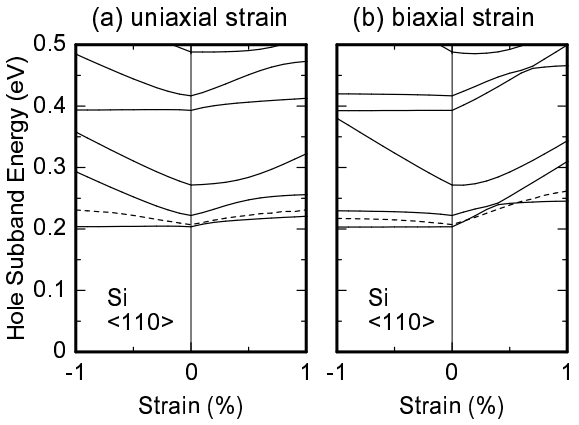

Fig. 8: Subband energies of 2D holes as a function of (a) uniaxial and (b) biaxial strain. The dashed lines represent the Fermi energies at $n_s = 1 \times 10^{13}$ cm^{-2}.

Figures 9 and 10 show μ and $v_{\rm inj}$ for Ge-pMOSFETs. The higher μ compared with the Si-channels, which has been also reported experimentally [1], is mainly due to the larger τ rather than the smaller m_c^* as is confirmed in Fig. 11. This originates from the larger energy splitting ($>\sim$ 100 meV) between the ground and the first excited subbands as shown in Fig. 12.

It is well known that the mobility of the unstrained pMOSFETs on (100) surface is isotropic because of the four-fold symmetry of the system [18]. This law does not apply to the injection velocity; in the case of Ge-channel, the anisotropy $v_{{\rm inj},\langle 110 \rangle} > v_{{\rm inj},\langle 100 \rangle}$ even in the unstrained condition can be clearly observed in Fig. 10, which originates from the warped valence band structure (see Fig. 13). On the other hand, as shown in Fig. 6, the anisotropy of $v_{\rm inj}$ for unstrained-Si channel is insignificant, because a relatively large fraction of holes occupy the excited as well as the ground subbands, and hence the Fermi energy is lower and the holes are distributed in the smaller area in k-space, where the band structure is not so warped.

The experimentally demonstrated higher current driv-

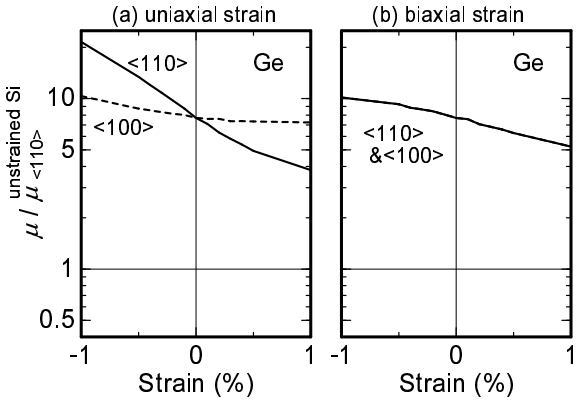

Fig. 9: μ of holes in Ge-pMOSFETs as a function of uniaxial and biaxial strain. The calculated results are normalized with respect to the values for the unstrained $\langle 110 \rangle$ Si-channel.

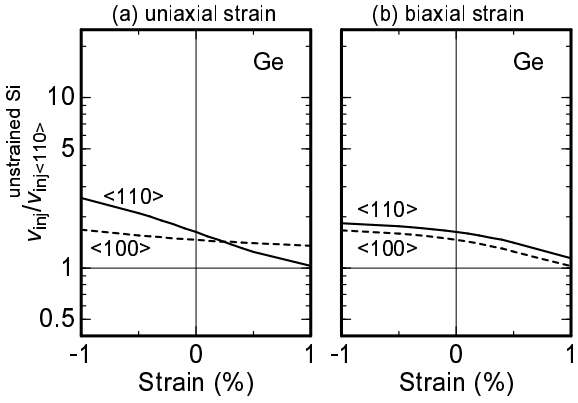

Fig. 10: $v_{\rm inj}$ of holes in Ge-pMOSFETs as a function of uniaxial and biaxial strain. The calculated results are normalized with respect to the values for the unstrained $\langle 110 \rangle$ Si-channel.

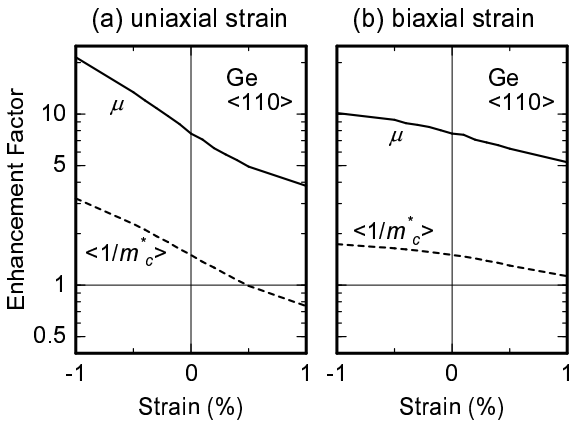

Fig. 11: μ and $\langle 1/m_c^* \rangle$ in $\langle 110 \rangle$ channel Ge-pMOSFETs as a function of (a) uniaxial and (b) biaxial strain. The calculated results are normalized with respect to the values for the unstrained $\langle 110 \rangle$ Si-channel.

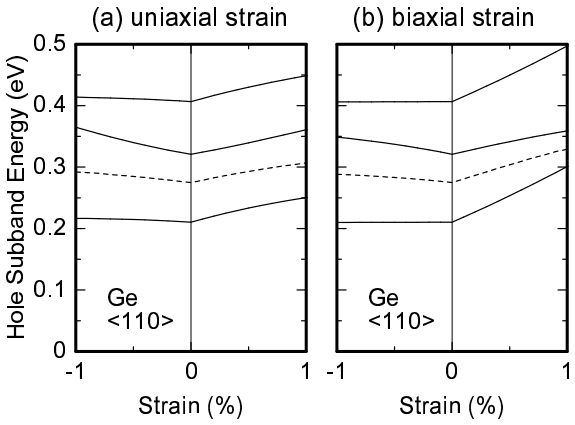

Fig. 12: Subband energies in $\langle 110 \rangle$ channel Ge-pMOSFETs as a function of (a) uniaxial and (b) biaxial strain. The dashed lines represent the Fermi energies at $n_s = 1 \times 10^{13}$ cm^{-2}.

ability of $\langle 100 \rangle$ rather than the conventional $\langle 110 \rangle$-channel [19] could be explained in terms of neither μ nor $v_{\rm inj}$. In order to clarify the mechanism of this observation, the information about more realistic electron distribution function than those assumed in this study (Fig. 3) is necessary, and the further investigations using, for example, the Monte Carlo simulations are required.

4. SUMMARY

We have numerically investigated the performance modulation of p-type Si- and Ge-MOSFETs with $\langle 110 \rangle$ and $\langle 100 \rangle$ channels under to the uniaxial and the biaxial strain. Both μ and $v_{\rm inj}$ are enhanced most effectively by the uniaxial compressive strain along the $\langle 110 \rangle$ channel. The contribution of τ and m_c^* on the mobility enhancement has been separately analyzed, and it has been shown that the enhancement of μ is more pronounced than $v_{\rm inj}$ due to the modulation of τ as well as m_c^*. Moreover, in Ge-channel the

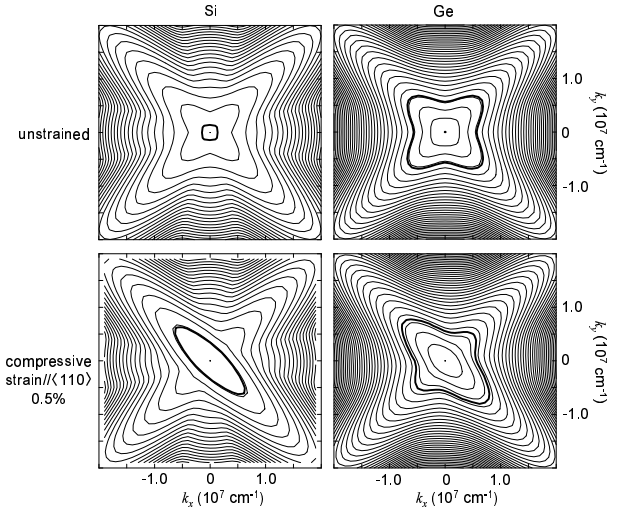

Fig. 13: Equienergy lines (step 20 meV) in the lowest subband for the Si- and Ge-channel pMOSFETs. The thick lines represent the Fermi surface at $n_s = 1 \times 10^{13}$ cm^{-2}.

higher μ can be expected compared with the Si-channels due to the larger τ, which originates from the larger subband splitting energy.

ACKNOWLEDGMENT

We are grateful to Prof. S. Takagi of Univ. of Tokyo for many valuable discussions and suggestions on the strained-Si MOSFET technology. We also acknowledge Prof. K. Matsuda of Naruto Univ. of Education for useful discussions on the physics of strained semiconductors. This work was supported by NEDO/MIRAI Project.

REFERENCES

[1] M. L. Lee et al., J.Appl.Phys. **97**, p011101 (2005).
[2] T.Ghani et al., Tech. Dig. IEDM, p978 (2003).
[3] T.Mizuno et al., Tech. Dig. IEDM, p31 (2002).
[4] S.M.Sze, *Physics of Semiconductor Devices 2nd ed.*,, (1981).
[5] H.Shang et al., IEEE Electron Device Letters, **24**, p242 (2003).
[6] H.Nakatsuji et al., Tech. Dig. IEDM, p727 (2002).
[7] M.V.Fischetti et al., J.Appl.Phys. **94**, p1079 (2003).
[8] K.Natori, J.Appl.Phys. **76**, p4879 (1994).
[9] S.Takagi, Symp. VLSI, p115 (2003).
[10] J.M.Luttinger et al., Phys.Rev. **97**, p869 (1955).
[11] G.L.Bir and G.E.Pikus, *Symmetry and Strain-Induced effects in Semiconductors*, (1974).
[12] C.Y.-P.Chao et al., Phys.Rev.B **46**, p4110 (1992).
[13] M.Lundstrom, IEEE Electron Device Letters. **18**, p361 (1997).
[14] M.M.Rieger et al., Phys.Rev.B **48**, p14276 (1993).
[15] P.Y.Yu and M.Cardona, *Fundamentals of Semiconductors*, Springer (1996).
[16] F.M.Bufler et al., J.Appl.Phys. **84**, p5597 (1998).
[17] H.Irie et al., Tech. Dig. IEDM, p225 (2004).
[18] K.Hess, *Advanced Theory of Semiconductor Devices*, Wiley-IEEE Press (1999).
[19] H.Sayama et al., Tech. Dig. IEDM, p657 (1999).